Numerical simulation of electrovortex flows in cylindrical fluid layers and liquid metal batteries

W. Herreman ⬤,[*] C. Nore ⬤, and P. Ziebell Ramos ⬤

Laboratoire d'Informatique pour la Mécanique et les Sciences de l'Ingénieur, LIMSI, CNRS, Univ. Paris-Sud, Université Paris-Saclay, Bât 507, Campus Universitaire F-91405 Orsay, France

L. Cappanera ⬤

Department of Computational and Applied Mathematics, Rice University, 6100 Main MS-134 Houston, Texas 77005, USA

J.-L. Guermond ⬤

Department of Mathematics, Texas A&M University 3368 TAMU, College Station, Texas 77843-3368, USA

N. Weber ⬤

Helmholtz-Zentrum Dresden-Rossendorf, Bautzner Landstrasse 400, 01328 Dresden, Germany

We use the multiphase magnetohydrodynamic code SFEMaNS to study the generation of electrovortex flows in liquid metal batteries. We first reproduce some well known results in a single-phase liquid metal column and then we characterize the electrovortex flow in layered multiphase fluid systems. A simple energy density balance argument accurately estimates the typical interface deformation caused by the electrovortex flow. When applied to Mg-Sb liquid metal batteries, we find that the electrovortex flows may have the capacity to cause short circuits even in moderate size batteries with radii in the range [10, 20] cm.

I. INTRODUCTION

Intermittent electrical energy sources, such as wind and solar energy, cannot have a significant impact on the global energy budget unless inexpensive and large-scale storage devices are put in place. Among the various options that are currently studied, liquid metal batteries (LMBs) have been identified to be viable candidates [1–3]. In this article, we study how the magnetohydrodynamic phenomenon known as electrovortex flow can impact the stably stratified structure of LMBs.

A sketch of a typical LMB configuration is shown in Fig. 1(a). A light liquid metal (represented with the letter A) is positioned on top of a medium density electrolyte composed of a molten salt, itself on top of a heavy liquid metal alloy that has a high affinity for A [represented by the symbols B(A)]. During discharge, electrons flow through the external circuit, while elements A dissolve as ions A^+ at the top of the electrolyte layer. At the bottom of the electrolyte, ions A^+ leave the electrolyte and alloy with B. As a result, the top layer of the LMB gets thinner and the bottom layer gets thicker during discharge. During charge the opposite mechanisms take place and the cell is restored to its original configuration. LMBs have attractive properties (low-cost materials, high energy efficiency, high-capacity retention, and high cyclability), but their main drawback is that they
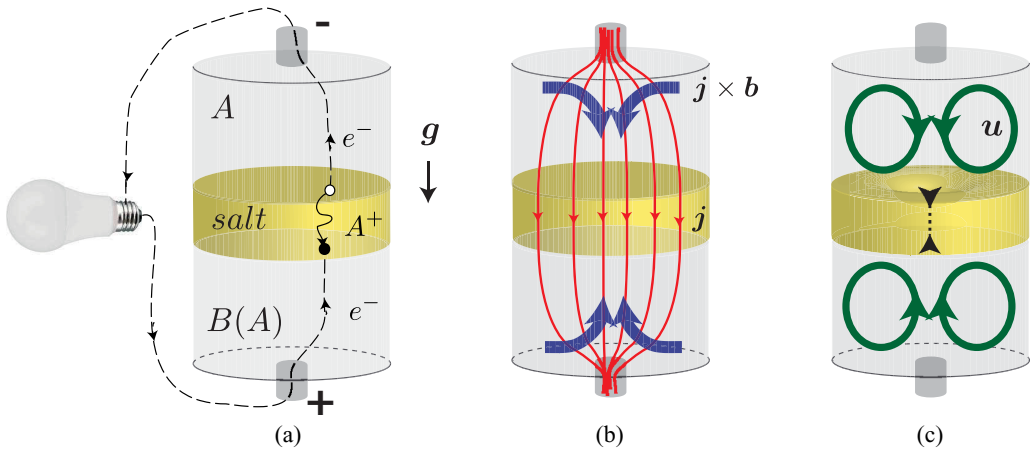
---

[*]wietze.herreman@limsi.fr

FIG. 1. A liquid metal battery (LMB) is composed of three layers of superposed conducting fluids with different densities. During discharge (a), electrons pass from the $-$ to the $+$ pole in the external circuit. Inside the battery, the top metal A dissolves as ions A^+ migrate downward in the electrolyte, and ultimately alloy with the bottom metal $B(A)$. (b) The shape of the current collectors causes the field lines of the electrical current j to spread out as they enter the top and the bottom layers. This causes an azimuthal magnetic field b and an inward Lorentz force $j \times b$. As a result an electrovortex flow u is created in both the top and the bottom layers, and this flow can deform the interfaces (c).

need to be heated ($\sim 400\,^\circ$C) to remain liquid. This certainly has an energetic cost, but not one that is prohibitive. Over the recent years, small LMB prototypes using inexpensive and Earth abundant materials have been built and tested [1–3]. The technology is presently being upscaled to allow a first phase of commercialization, but further studies are needed to reveal the full possibilities and limitations of the LMB technology.

The design of new LMB prototypes is necessary, but it is also interesting to use numerical simulations as a complementary tool to get insights in the chemical and physical processes occurring inside these cells. Fluid motions, of hydrodynamical, thermal or magnetohydrodynamical origin are unavoidable in LMBs and have received a particular attention (natural convection [4–8], the Tayler instability [9–11], the metal pad roll instability [12–19], and the electrovortex flow [4,7,10,20]). Too intense flows need to be avoided as they can compromise the stable stratification of the battery. However, flows can also be desirable. In the alloy layer, flows will improve the mixing limiting mass transfer overpotentials [2,4] or will prevent the formation of undesirable (solid) intermetallic phases. We refer the reader to Ref. [9] where safety issues connected to magnetohydrodynamic instabilities are discussed and to Ref. [21] for a recent review of flows in LMBs.

In this article, we continue this research of fluid flows in LMBs, focusing on the so-called electrovortex flow (EVF). EVF commonly arises in liquid metal regions that are in contact with thinner solid electrodes; see Ref. [22] for a detailed overview. Due to a difference in shape between the solid electrode and the liquid metal bath, the field lines of the electrical current j spread out as sketched in Fig. 1(b). Along with this current comes a magnetic induction b and a Lorentz force $j \times b$ that effectively pushes the liquid metal away from the solid electrodes toward less intense j regions, see Ref. [23]. Inside a LMB, strong enough EVF can deform the interfaces separating the fluid layers and potentially even cause short circuits, see Fig. 1(c). The objective of this paper is to characterize the intensity of the EVF inside multiphase systems, such as a LMBs and to asses whether EVF may cause short circuits. The investigation is done numerically by using the massively parallel, multiphase, magnetohydrodynamic code SFEMaNS (the acronym stands for Spectral/Finite Element code for Maxwell and Navier-Stokes equations). This code uses cylindrical coordinates and is well suited to study the EVF in axisymmetric domains. Full details

on the numerical method that is used are given in Ref. [24]. The multiphase algorithm in SFEMaNS has been benchmarked with OpenFOAM on the metal pad roll problem in Ref. [19].

The article is structured as follows. In Sec. II, we first present our solver SFEMaNS used for the computations. In Sec. III, we study the EVF in a single fluid layer to recover some well-known results and scaling laws in axisymmetric context and in three-dimensional simulations. We also investigate how a realistic solid electrode affects EVF and this allows to discuss the accuracy of commonly used idealized boundary conditions (see Refs. [22,25]). In Sec. IV, we study the EVF in setups composed of two and three layers of conducting fluids and in particular, the Mg-Sb LMB [1]. We calculate typical flow intensities and estimate the amplitude of the deformation of the interfaces caused by EVF. Using similitude principles, we then estimate typical battery sizes for which the EVF mechanism may become very intense and thereby compromise the stratified structure of the battery.

II. SFEMANS SOLVER

The numerical study presented here is done using the spectral/finite element code for Maxwell and Navier-Stokes equations (SFEMaNS). This magnetohydodynamic (MHD) solver was developed in 2001 and was initially designed to study dynamo problems in axisymmetric fluid domains. The numerical method for monophase fluid domains was previously described in Refs. [26–28] and has been thoroughly validated on numerous manufactured solutions and against other magnetohydrodynamic codes (see, e.g., Refs. [27,29]). The code has now been extended to allow for multiple liquid metal phases, allowing the simulations of Ref. [11] on the Tayler instability in liquid metal batteries. The numerical method is fully detailed in Ref. [24]. In recent work on the metal pad roll instability in reduction cells [19], we have shown that multiphase MHD simulations done with SFEMaNS and an entirely different code (OpenFOAM, also used in Ref. [30]) almost yield identical results that are further in quantitive agreement with a linear stability theory. Here we use SFEMaNS for the first time to study electrovortex flows in multiphase setups.

Let us present the numerical method used by SFEMaNS in a nutshell (all numerical details are available in the mentioned references). Denoting by $\rho, \boldsymbol{m} = \rho\boldsymbol{u}, p$, and $\boldsymbol{b}$ the density, the momentum, the pressure, and the magnetic field, respectively, the conservation of mass, the conservation of momentum, the solenoidality of the magnetic field, and the induction equation are expressed as follows in dimensional form:

$$\partial_t \rho + \boldsymbol{\nabla} \cdot \boldsymbol{m} = 0, \tag{1a}$$

$$\boldsymbol{\nabla} \cdot \boldsymbol{u} = 0, \tag{1b}$$

$$\partial_t \boldsymbol{m} + \boldsymbol{\nabla} \cdot (\boldsymbol{m} \otimes \boldsymbol{u}) - \boldsymbol{\nabla} \cdot (\eta(\boldsymbol{\nabla}\boldsymbol{u} + \boldsymbol{\nabla}\boldsymbol{u}^T) + \boldsymbol{\nabla} p = -\rho g \boldsymbol{e}_z + \frac{(\boldsymbol{\nabla} \times \boldsymbol{b}) \times \boldsymbol{b}}{\mu_0}, \tag{1c}$$

$$\boldsymbol{\nabla} \cdot \boldsymbol{b} = 0, \tag{1d}$$

$$\partial_t \boldsymbol{b} + \boldsymbol{\nabla} \times \left(\frac{\boldsymbol{\nabla} \times \boldsymbol{b}}{\mu_0 \sigma}\right) = \boldsymbol{\nabla} \times (\boldsymbol{u} \times \boldsymbol{b}). \tag{1e}$$

Here g is gravity and $\boldsymbol{e}_z$ conventionally gives the unit vector in the upward direction. μ_0 is the vacuum permeability, ρ, η, σ material parameters of the liquid metal, respectively, density, dynamic viscosity, and electrical conductivity. SFEMaNS solves these equations in arbitrary axisymmetric fluid domains, potentially surrounded by current-free regions or other solid conductors. When only one phase is present, material parameters remain constant. Liquid metal batteries include more than one fluid. The presence of multiple phases is accounted by using a level set technique. The material parameters ρ, η, and $1/\sigma$ are space and time-dependent fields that are reconstructed using level set functions [24]. For example, in a two-phase case (indices 1 and 2), the density is given by $\rho = \rho_2 + (\rho_1 - \rho_2)\phi = \rho_2(1 - \phi) + \rho_1\phi$ with $\phi \in [0, 1]$ the sharply varying level set function that

TABLE I. Details on the numerical simulations discussed in this article. Referring to each figure, we provide the number of Fourier modes M, mesh size (uniform), or interval (nonuniform) of mesh sizes of the finite element grid in the meridional plane. In all simulations, the time step Δt is fixed. Intervals $\ldots \rightarrow \ldots$ indicate how Δt was changed with increasing S (or current I).

Figures	M	Mesh size	Δt	Figures	M	Mesh size	Δt
3, 4(a), 5	1	[0.01, 0.025]	10^{-3}	11, 12	1	[0.25, 1] mm	$5 \times 10^{-4} \rightarrow 10^{-4}$ s
4(b)	1	0.005	10^{-3}	13	1	[0.25, 1] mm	10^{-4} s
4(b)	1	0.01	10^{-3}	14	1	[0.25, 1] mm	2.5×10^{-5} s
4(b)	1	0.05	10^{-3}	15 (real)	1	[0.25, 1] mm	2.5×10^{-5} s
6, 7, 8	1	[0.01,0.025]	$10^{-2} \rightarrow 4 \times 10^{-7}$	15 (fake)	1	[0.25, 1] mm	7.5×10^{-5} s
9, 10	16	[0.005,0.01]	$10^{-5} \rightarrow 2.5 \times 10^{-7}$	16	1	[0.25, 1] mm	$5 \times 10^{-4} \rightarrow 2.5 \times 10^{-5}$ s

is materially advected by the flow $\boldsymbol{u}$:

$$\partial_t \phi + (\boldsymbol{u} \cdot \boldsymbol{\nabla})\phi = 0, \tag{2}$$

In the three-layer case, two level set functions are used such that, e.g., $\rho_{21}(\phi_1) = \rho_2(1 - \phi_1) + \rho_1\phi_1$ and $\rho = \rho_3(1 - \phi_2) + \rho_{21}(\phi_1)\phi_2$, where $\phi_1 \in [0, 1]$ varies steeply across the interface between the top layer (1) and the electrolyte (2), and $\phi_2 \in [0, 1]$ varies sharply across the interface between the electrolyte (2) and the bottom layer (3). Both ϕ_1, ϕ_2 are then materially advected. A compression technique is used to keep the interfaces sharp (typically smeared out over some 3 gridpoints, but not more). The present version of the code handles capillary pressure jumps on the interfaces but does not model contact lines properly [regions where 3-phases encounter (solid-liquid-liquid) or (liquid-liquid-liquid)]. Therefore, we ignore capillary effects in the simulations that follow. Equations presented above are dimensional, but SFEMaNS can also be used in nondimensional form.

Having supposed an axisymmetric fluid domain, we may discretize the system of Eqs. (1) using a Fourier decomposition in the azimuthal θ direction. In the meridian (r, z) section, we use continuous finite elements ($\mathbb{P}_1$ Lagrange elements for the pressure and $\mathbb{P}_2$ Lagrange elements for the velocity and the magnetic field). As an example, the approximate velocity field then has the following representation:

$$\boldsymbol{u} = \sum_{m=0}^{M-1} \boldsymbol{u}_m^c(r, z, t) \cos(m\theta) + \sum_{m=1}^{M-1} \boldsymbol{u}_m^s(r, z, t) \sin(m\theta), \tag{3}$$

where $\boldsymbol{u}_m^c(r, z, t)$ and $\boldsymbol{u}_m^s(r, z, t)$ are vector-valued finite elements functions. All the fields, either vector-valued or scalar-valued, are represented as above. M is the number of Fourier modes used in the discretization. In the axisymmetric simulations, we use $M = 1$. Three-dimensional simulations require more modes but we found that $M = 16$ is suitable. All simulations are initialized with fluid at rest and are of course subject to numerical discretization errors. Initial magnetic field conditions are not very important as the magnetic field almost immediately adjusts in one or two time steps. Modulo the computation of nonlinear terms using FFTW3, the handling of the Fourier modes in the meridian plane, (r, z), can be done in parallel and we also use parallel domain decomposition strategies. The divergence of $\boldsymbol{b}$ is controlled by a technique using a negative Sobolev norm that guarantees convergence under minimal regularity (see details in Refs. [31], [[32], Sec. 3.2], and [33]).

In Table I, we provide details on the numerical simulations presented in this article. Referring to each of the figures, we provide the number of Fourier modes M, the mesh size (uniform), or interval of mesh sizes (nonuniform) of the finite element grid in the meridional plane. The time step Δt is also provided and remains fixed in our simulations. Examples of meridional meshes are shown in
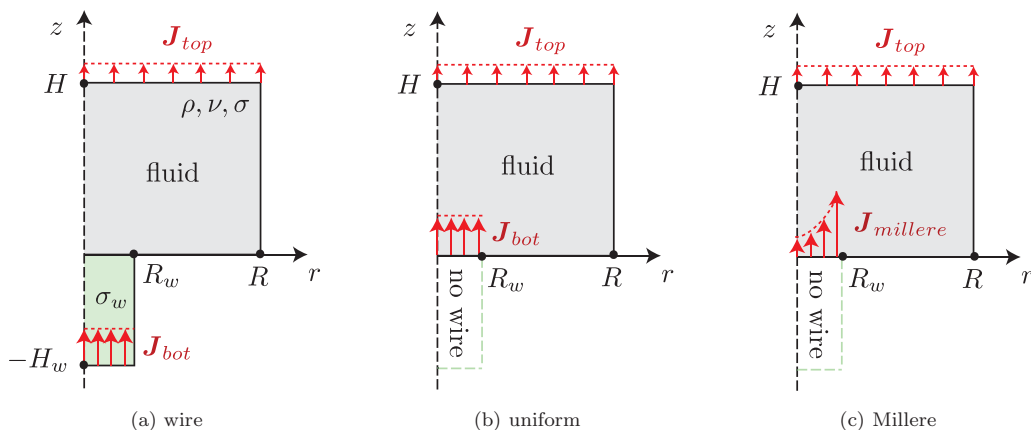
FIG. 2. Computational domains used to study the EVF in a liquid metal column. On top of the fluid domain, we suppose a homogeneous current density J_{top}. Three different setups are compared. In setup (a), the fluid is connected electrically to a solid wire which is fed from below with a homogeneous current density J_{bot}. In setup (b), there is no wire and a homogeneous current density J_{bot} directly enters the fluid domain. In setup (c), the wire is modeled by using a particular Millere current density profile [see Eq. (4)] over the section where the wire should be connected to the liquid bath.

Figs. 3(e) and 13(b). A convergence study is done on a particular setup and this is further discussed below [see Fig. 4(b)].

III. ELECTROVORTEX FLOW IN A SINGLE FLUID LAYER

A. Geometry and equations

We consider an incompressible liquid metal with kinematic viscosity ν and density ρ. The fluid domain is a cylinder of radius R and height H. The total electrical current I runs vertically through the system. This current enters at the bottom and is connected to the fluid through a section of radius R_w. The current exits at the top across the entire section of radius R. The chosen geometry is one of the classical examples of electrovortex flow investigated in the literature, theoretically [25,34–36], numerically [30,37,38], and experimentally [39,40].

We study three different setups sketched in Fig. 2. In all the setups we suppose that the current density on the top section is homogeneous, $J_{\text{top}} = (I/\pi R^2)e_z$. In setup (a), the fluid is electrically connected to a solid wire of height H_w and conductivity σ_w which is fed from below with a uniform current density $J_{\text{bot}} = (I/\pi R_w^2)e_z$. In setup (b), referred to as the uniform case, there is no wire and a homogeneous current density J_{bot} directly enters the fluid domain. In setup (c), referred to as the Millere case, there is no wire either, but, using cylindrical coordinates, we suppose that the current distribution has the form

$$J_{\text{Millere}} = \frac{I}{2\pi R_w^2} \frac{1}{\sqrt{1 - (r/R_w)^2}} \, e_z \tag{4}$$

and enters through the cylindrical section $\{0 \leqslant r \leqslant R_w\}$. This particular current density profile has been used in Refs. [22,25]; it corresponds to the current density that would be observed at the surface of a flat, perfectly conducting electrode of radius R_w, feeding a current I to a semi-infinite conductor. We expect that this distribution is a reasonable approximation for a thin well-conducting wire connected to a large fluid domain, i.e., when $\sigma_w \gg \sigma$, $R_w \ll R$, $R_w \ll H$.

We nondimensionalize the problem using the following scales for space, time, velocity, pressure, and magnetic field:

$$[\boldsymbol{r}] = R, \quad [t] = \frac{R^2}{\nu}, \quad [\boldsymbol{u}] = \frac{\nu}{R}, \quad [p] = \frac{\rho \nu^2}{R^2}, \quad [\boldsymbol{b}] = \frac{\mu_0 I}{2\pi R}, \tag{5}$$

with μ_0 the magnetic permeability of vacuum. For brevity, we abuse the notation by not changing the notation for the nondimensional variables, e.g., (r, θ, z) designate the nondimensionalized, cylindrical coordinates. Three geometric nondimensional parameters are fixed:

$$h = \frac{H}{R} = 1, \quad h_w = \frac{H_w}{R} = 1, \quad r_w = \frac{R_w}{R} = 0.2. \tag{6}$$

The following three remaining nondimensional parameters are allowed to vary:

$$S = \frac{\mu_0 I^2}{4\pi^2 \rho \nu^2}, \quad P_m = \sigma \mu_0 \nu, \quad \hat{\sigma} = \frac{\sigma_w}{\sigma}. \tag{7}$$

The number S measures the ratio between the magnetic and the viscous forces and is referred to as the EVF parameter in Ref. [7]. P_m is the magnetic Prandtl number of the fluid. $\hat{\sigma}$ is the ratio of electrical conductivities of the wire and the fluid. The nondimensional magnetohydrodynamic equations to be satisfied in the fluid are

$$\partial_t \boldsymbol{u} + (\boldsymbol{u} \cdot \nabla)\boldsymbol{u} = -\nabla p + \Delta \boldsymbol{u} + S(\nabla \times \boldsymbol{b}) \times \boldsymbol{b}, \tag{8a}$$

$$\partial_t \boldsymbol{b} = \nabla \times (\boldsymbol{u} \times \boldsymbol{b}) + P_m^{-1} \Delta \boldsymbol{b}, \tag{8b}$$

$$\nabla \cdot \boldsymbol{u} = 0, \tag{8c}$$

$$\nabla \cdot \boldsymbol{b} = 0. \tag{8d}$$

Moreover, in setup (a) described in Fig. 2 we solve the induction equation in the wire:

$$\partial_t \boldsymbol{b}_w = (\hat{\sigma} P_m)^{-1} \Delta \boldsymbol{b}_w, \tag{9a}$$

$$\nabla \cdot \boldsymbol{b}_w = 0. \tag{9b}$$

Occasionally we will use the notation $\boldsymbol{j} := \nabla \times \boldsymbol{b}$, $\boldsymbol{j}_w := \nabla \times \boldsymbol{b}_w$ for the electrical current densities in the fluid and in the wire, respectively. On the boundaries of the fluid domain we enforce the no-slip condition:

$$\boldsymbol{u}|_{r=1} = \boldsymbol{u}|_{z=1} = \boldsymbol{u}|_{z=0} = \boldsymbol{0}. \tag{10}$$

In wire setup (a), there is internal boundary at the electrical contact and there we use the physical boundary conditions

$$\boldsymbol{e}_z \times (\boldsymbol{b} - \boldsymbol{b}_w)|_{z=0} = 0, \quad \boldsymbol{e}_z \times (\boldsymbol{j} - (\boldsymbol{j}_w/\hat{\sigma}))|_{z=0} = 0, \quad \forall r \in [0, r_w], \tag{11}$$

expressing continuity of tangential magnetic and electrical fields. On any point of the outer boundary, we need to have

$$b_\theta|_{r=r_b} = \frac{1}{r_b} \int_0^{r_b} j_z r \, dr, \tag{12}$$

according to Ampère's law, and this yields

$$b_\theta|_{r=1} = 1, \quad \forall z \in [0, 1]; \quad b_\theta|_{z=h} = r, \quad \forall r \in [0, 1]; \quad b_\theta|_{z=0} = 1/r, \quad \forall r \in [r_w, 1], \tag{13a}$$

and depending on the setup

$$\text{(a) wire :} \quad b_{w,\theta}|_{r=r_w} = 1/r_w, \quad \forall z \in [-h_w, 0]; \quad b_{w,\theta}|_{z=-h_w} = r/r_w^2, \quad \forall r \in [0, r_w], \tag{13b}$$

$$\text{(b) uniform}: \quad b_\theta|_{z=0} = r/r_w^2, \quad \forall r \in [0, r_w], \tag{13c}$$

$$\text{(c) Millere}: \quad b_\theta|_{z=0} = (1 - \sqrt{1 - (r/r_w)^2})/r, \quad \forall r \in [0, r_w]. \tag{13d}$$

The boundary condition in setup (c) is obtained by using Eq. (4) in Eq. (12). These boundary conditions for b_θ are all we need in axisymmetric simulations, since $b_r = b_z = 0$ everywhere for an isolated device placed in a current-free exterior. The Millere condition is often given in the literature in the form of Eq. (13d); it is rarely formulated in the form of Eq. (4). This condition is obtained by solving $\nabla \times \nabla \times (b_\theta \boldsymbol{e}_\theta) = -\Delta(b_\theta \boldsymbol{e}_\theta) = \boldsymbol{0}$ in oblate spheroidal coordinates in an infinite fluid domain above a perfectly conducting disk (see Ref. [22] for details). One then derives Eq. (13d) by expressing the solution thus obtained on the surface of the disk using cylindrical coordinates. Notice that, unlike the Millere current density, the Millere azimuthal magnetic field profile is not singular at $r = r_w$.

We also investigate how EVF becomes three-dimensional and in these three-dimensional simulations, $b_r, b_z \neq 0$. Extra magnetic boundary conditions on the outer surface are then required by the calculation. For the sake of simplicity, we suppose that tangential field components other than b_θ vanish, meaning $b_r = 0$ on all horizontal outer boundaries and $b_z = 0$ on all vertical outer boundaries. Similar boundary conditions were also used in Ref. [11] and had little impact there, but strictly speaking, they are not correct for a device surrounded by a current-free exterior. Let us estimate the impact of this idealized boundary condition. All our three-dimensional simulations are done in the low Rm regime: $\mathrm{Rm} = \sigma \mu_0 U_{\max} R < 10^{-3}$ maximally in what follows. In this low Rm limit, the magnetic field is $\boldsymbol{b} \approx b_\theta^{\mathrm{ms}}(r, z)\boldsymbol{e}_\theta + O(\mathrm{Rm})$, where the dominant magnetostatic part satisfies $\Delta[b_\theta^{\mathrm{ms}}(r, z)\boldsymbol{e}_\theta] = 0$. Boundary conditions on b_r, b_z, realistic or approximated, have no influence on $b_\theta^{\mathrm{ms}}(r, z)$ and can only modify the much smaller, $O(\mathrm{Rm})$ part of the magnetic field (the quasi-static field correction). As a consequence, we can estimate that the Lorentz force $(\nabla \times \boldsymbol{b}) \times \boldsymbol{b}$ and the electrovortex flow it drives, can only be affected by $O(\mathrm{Rm})$ relative differences in the low Rm limit. Implementing realistic boundary conditions would require the calculation of external magnetic field, an expensive extra computational effort, but one with very low impact on EVF. This explains our preference for idealized boundary conditions on b_r, b_z, in three-dimensional simulations.

B. Axisymmetric study

In this section, we impose axisymmetry: All fields are θ-independent and $b_r = b_z = j_\theta = j_{w,\theta} = u_\theta = 0$.

1. Spatial structure of current density, Lorentz force, and electrovortex flow

As a first example, we focus on the setup with a wire that has the same conductivity as the liquid metal, $\hat{\sigma} = 1$ and further fix $P_m = 0.2$, $S = 250$. This choice of parameters is not inspired by a realistic setup, but it allows us to compare with previous simulations [[22], p. 187]. Starting with the fluid at rest, a stationary flow is reached after a short transient. In Fig. 3(a) we show a collection of streamlines of the stationary electrovortex flow in a meridional plane. A vertical jet directed away from the bottom electrode recirculates along the lateral wall. The flow is the most intense on the axis. Fig. 3(b) shows how the electrical current density spreads out from the bottom section to the top section. Figure 3(c) shows the field lines of the associated Lorentz force. Notice that this force is very large close to the point $(r, z) = (0.2, 0)$. When looking at this picture, it is not immediately clear how the Lorentz force can create the electrovortex flow. Actually only part of the Lorentz force contributes to the generation of the flow. Recalling that $b_r = b_z = 0$, we rewrite the Lorentz force as

$$\boldsymbol{j} \times \boldsymbol{b} = -\frac{b_\theta^2}{r}\boldsymbol{e}_r - \frac{1}{2}\nabla b_\theta^2. \tag{14}$$

We thus separate a potential part $-\nabla b_\theta^2/2$, which only modifies the pressure, from the quantity $-(b_\theta^2/r)\boldsymbol{e}_r$, which effectively drives the electrovortex flow. The spatial distribution of $-(b_\theta^2/r)\boldsymbol{e}_r$
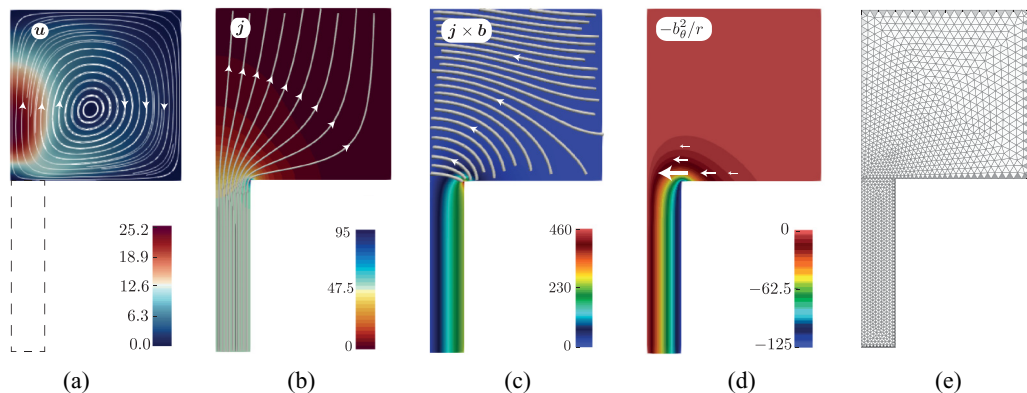
FIG. 3. Steady-state fields in the wire setup for $S = 250$, $P_m = 0.2$, $\hat{\sigma} = 1$. (a) Electrovortex flow and intensity in color code. (b) Field lines and magnitude of the electrical current density $\boldsymbol{j}$. (c) Lorentz force $\boldsymbol{j} \times \boldsymbol{b}$ and intensity. Notice the concentration near $(r, z) = (0.2, 0)$. (d) Part of the Lorentz force $-(b_\theta^2/r)\boldsymbol{e}_r$ that effectively drives the flow. Vectors suggest magnitude and direction but are not at scale. (e) Numerical grid used in the computations.

is shown in Fig. 3(d). Arrows (not at scale) suggest the radially inward direction and relative magnitude. This figure suggests better than Fig. 3(c) that the fluid is being pushed toward the axis in the immediate vicinity of the bottom contact. It is the action of the force $-(b_\theta^2/r)\,\boldsymbol{e}_r$ combined with the incompressibility of the fluid that yields the fluid flow sketched in Fig. 3(a). Figure 3(e) shows the nonuniform grid used in our computations, with mesh sizes varying in the interval $[0.01, 0.025]$.

2. With or without wire

We consider setup (a) of Fig. 2 with wires of different conductivities, a badly conducting wire $\hat{\sigma} = 0.01$, a wire with the same conductivity as the liquid metal $\hat{\sigma} = 1$ and a case $\hat{\sigma} = 56$ in which the conductivity ratio is that of copper to mercury. We compare these simulations to the simplified models (b) and (c) without wire (uniform and Millere cases). We fix $S = 25$, $P_m = 0.2$ in this section, also studied in Ref. [[22], p. 187]. In Fig. 4(a), we show the vertical flow $u_z(0, z)$ along the axis. All the curves have similar profiles. The uniform model yields the most intense flow, and we observe that it is well adapted to model the effect of a wire with low relative conductivity ($\hat{\sigma} \ll 1$). The Millere setup yields a less intense flow, and we observe that it is well adapted to model wires with high relative conductivity ($\hat{\sigma} \gg 1$). For wires with conductivities in the same range as the fluid ($\hat{\sigma} \approx 1$), the intensity of the flow is between that produced by the models (b) and (c). The Millere curve in Fig. 4(a) can be compared to the results provided in Ref. [[22], p. 187]. Our results are not exactly identical but are qualitatively similar. To ascertain the accuracy of our computations, we show in Fig. 4(b) results with the Millere setup obtained on three different meshes. It seems clear that the results presented here are very close to convergence.

The relative conductivity of the wire has a strong impact on the vertical current density near the electrical contact. This is shown in Fig. 5(a): j_z evolves from an almost uniform profile in the case $\hat{\sigma} \ll 1$, toward the concentrated, Millere-like profile in the limit $\hat{\sigma} \gg 1$. Figure 5(b) shows that, unlike j_z, b_θ is only weakly affected by $\hat{\sigma}$. Varying $\hat{\sigma}$, the field b_θ varies in the immediate neighborhood of the small wedge delimited by the Millere and uniform cases. Since b_θ is slightly more intense in the uniform setup (i.e., $\hat{\sigma} \ll 1$), and since the EVF is effectively forced by $-(b_\theta^2/r)\,\boldsymbol{e}_r$, we now understand why low values of $\hat{\sigma}$ yield slightly more intense EVF as observed in Fig. 4(a). Since the Lorentz force $\boldsymbol{j} \times \boldsymbol{b}$ is as sensitive to $\hat{\sigma}$ as j_z, its magnitude $\|\boldsymbol{j} \times \boldsymbol{b}\|$ can therefore reach very high values near the electrodes in the limit $\hat{\sigma} \gg 1$; this phenomenon is
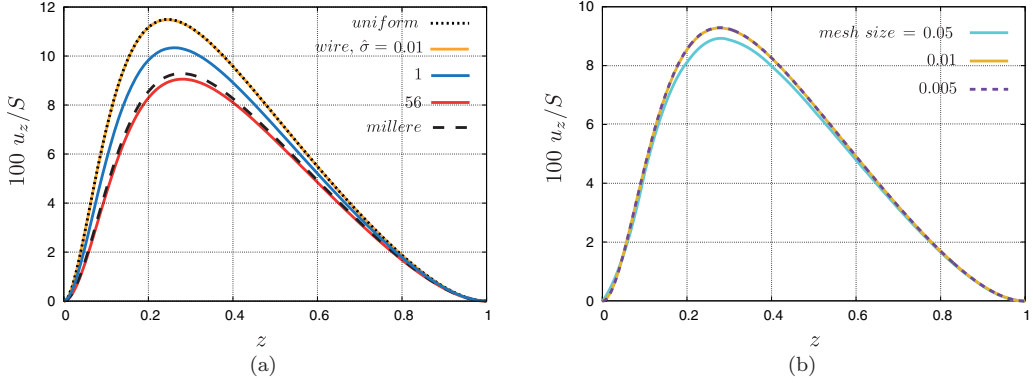
FIG. 4. Vertical velocity on the axis $r = 0$ for setups (a), (b), and (c) of Fig. 2, all obtained with $S = 25$, $P_m = 0.2$. (a) At low wire conductivity ($\hat{\sigma} \ll 1$), the uniform current inlet model is well-adapted and the EVF the most intense. At high wire conductivity ($\hat{\sigma} \gg 1$), Millere's boundary condition is adequate and the EVF is the least intense. For $\hat{\sigma} \simeq 1$ the flow intensity ranges between those given by models without wire (uniform and Millere cases). (b) Convergence study for the Millere setup on uniform meshes with varying mesh size.

already visible in Fig. 3(c) for $\hat{\sigma} = 1$. Notice, however, that this singular behavior mainly affects the pressure in the fluid and not so much the intensity of the electrovortex flow.

3. Varying S

We calculate the electrovortex flow for various values of S in the range $[6.25, 5 \times 10^6]$ and with $P_m \in \{0, 10^{-6}, 0.2\}$. The case $P_m = 0$ corresponds to the magnetostatic limit in which $\Delta(b_\theta e_\theta) = 0$ and is an idealization of $P_m = 10^{-6}$, a realistic value for liquid metals. The case $P_m = 0.2$ allows us to observe how inductive effects can influence EVF. We restrict ourselves to the Millere boundary condition in this section. We introduce a Reynolds number of the electrovortex flow based on the maximal flow speed in the fluid. Given our choice of length and timescale, this number measures
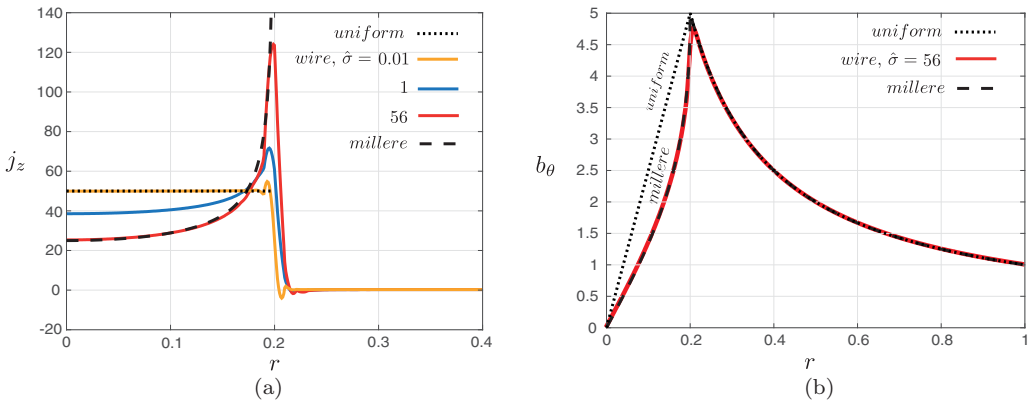

FIG. 5. Current density j_z and azimuthal magnetic field b_θ at the bottom electrical contact $z = 0$ with or without wire ($S = 25$, $P_m = 0.2$). (a) The current density j_z strongly depends on the conductivity of the wire. The (singular) Millere current density profile is adequate for high $\hat{\sigma} \gg 1$, the uniform current density is adequate for low $\hat{\sigma} \ll 1$. (b) The magnetic field b_θ is only weakly affected by $\hat{\sigma}$. The differences between the results obtained with the Millere and the uniform boundary conditions are small.
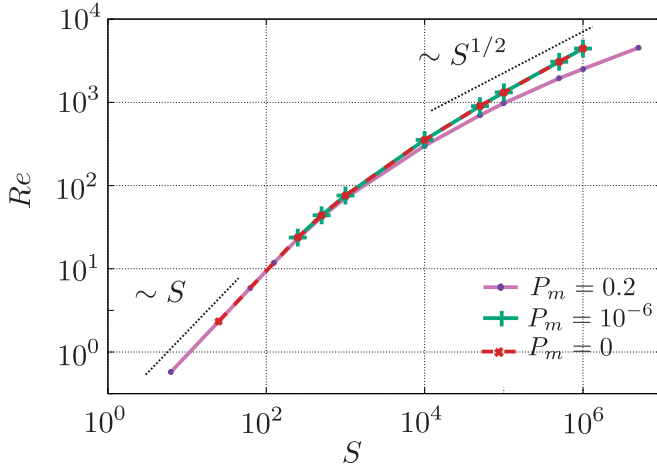
FIG. 6. Reynolds number of the electrovortex flow based on the maximal speed, as a function of S and for various P_m. When S is small, we observe the scaling law Re $\sim S$ for all P_m. When S is large, we observe Re $\sim S^{1/2}$ for low values of P_m. Millere's boundary conditions are used at the current inlet.

the flow intensity,

$$\text{Re} = \frac{U_{\max}R}{\nu} = \max_{\boldsymbol{x},t}(\|\boldsymbol{u}\|). \tag{15}$$

We show in Fig. 6 the Reynolds number as a function of S in logarithmic scale (for the three values $P_m \in \{0, 10^{-6}, 0.2\}$). We observe that Re (i.e., the flow intensity) monotonically increases with S. We observe that the flow at high values of S is weaker for $P_m = 0.2$ than for $P_m = 0$. For low values of P_m, we observe the following scaling laws:

$$\text{low } S \text{ range}: \quad \text{Re} \sim S, \quad \text{high } S \text{ range}: \quad \text{Re} \sim S^{1/2}. \tag{16}$$

These scaling laws when P_m is small are well known [22]. They can be inferred from the momentum Eq. (8a). The force density $-(S\,b_\theta^2/r)\,\boldsymbol{e}_r$ which drives the EVF is proportional to S. Recalling that we are working with nondimensional equations, for low intensity flows, i.e., in the Stokes limit, this force is balanced by the viscous diffusion, $\|\Delta\boldsymbol{u}\| \sim S$, which yields $\|\boldsymbol{u}\| \sim S$ or Re $\sim S$. For high intensity flows, inertia takes over and we instead have $\|(\boldsymbol{u} \cdot \boldsymbol{\nabla})\boldsymbol{u}\| \sim S$ yielding $\|\boldsymbol{u}\| \sim \sqrt{S}$ or Re $\sim \sqrt{S}$. Bojarevics [22] proposed the following refinements of these scaling laws when P_m is small to take into account the size r_w of the wire:

$$\text{Re} = \begin{cases} S\,(10^{1+5r_w})^{-1/2} & \text{for } S < 10^3, \\ \sqrt{S}\,(10^{3-5r_w})^{1/3} & \text{for } S > 10^5. \end{cases} \tag{17}$$

Using $r_w = 0.2$, this gives Re $= 0.1 \times S$ for $S < 10^3$, and Re $= 4.64 \times S^{1/2}$ for $S > 10^5$. Let us compare these theoretical predictions to our numerical results, which we recall are all done with $r_w = 0.2$.

In Fig. 7 we display the vertical velocity along the axis ($r = 0$), rescaled by S in the low S regime [Fig. 7(a)] and rescaled by $S^{\frac{1}{2}}$ in the high S regime [Fig. 7(b)]. In the low S regime, the law Re $\approx 0.1\,S$ is well adapted up to 4% for both low and high values of P_m. In the high S regime, we find that Re $\approx 4.64\,S^{1/2}$ is well adapted up to 3% for low values of P_m. Notice that spatial profiles of the velocity are different in the low S regime and in the high S regime. The maximum of the velocity profile is close to the wire when S is small, but the location of the maximum moves away from the wire as S increases.
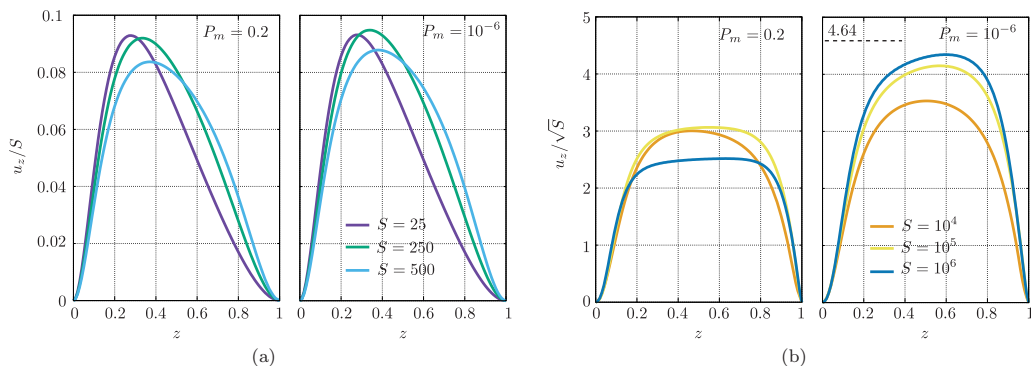
FIG. 7. Rescaled vertical velocity profiles along the axis $r = 0$ for various values of S and $P_m \in \{10^{-6}, 0.2\}$ and using Millere boundary conditions. (a) In the low S range: velocity profiles rescale well as u_z/S for both values of P_m. (b) In the high S range: velocity profiles rescale well as $u_z/\sqrt{S}$.

The results shown in Figs. 6 and 7 suggest that for high values of P_m and high values of S, the scaling law Re $\sim \sqrt{S}$ is no longer appropriate. This is due to inductive effects, i.e., the term $\nabla \times (\boldsymbol{u} \times \boldsymbol{b})$ reaches the same order of magnitude as the diffusive term $P_m^{-1}\Delta \boldsymbol{b}$ when Re $\sim P_m^{-1}$ or, alternatively, when the magnetic Reynolds number Rm $= \sigma \mu_0 U_{\max} R$ is of order 1. In real liquid metals, where $P_m \sim 10^{-6} - 10^{-7}$ is typical, inductive effects have very little impact unless S is extremely large.

Some further information on how the flow changes as S increases is given in Fig. 8. We show streamlines and color maps of the magnitude of the velocity for $S \in \{500, 10^4, 5 \times 10^4, 5 \times 10^5\}$. The streamlines are rather symmetrical at low values of S, but symmetry breaks as S increases and we clearly see two phenomena happening when S is large. First, the fluid is ejected upward so energetically that it hits the upper wall at right angle and gets violently ejected outward in a thin layer that is almost as fast as the vertical jet. Second, the center of the main vortex moves toward the upper-right corner, and the fluid in the bottom-right corner becomes stagnant. The structure of the weak recirculation zone that appears in the bottom-right corner around $S \sim 5 \times 10^4$ becomes gradually more complex as S increases.

C. Three-dimensional study

In this section we get rid of the axisymmetry assumption. The force that drives EVF only acts on the axisymmetric flow-component but three-dimensional features may arise by instabilities. In our
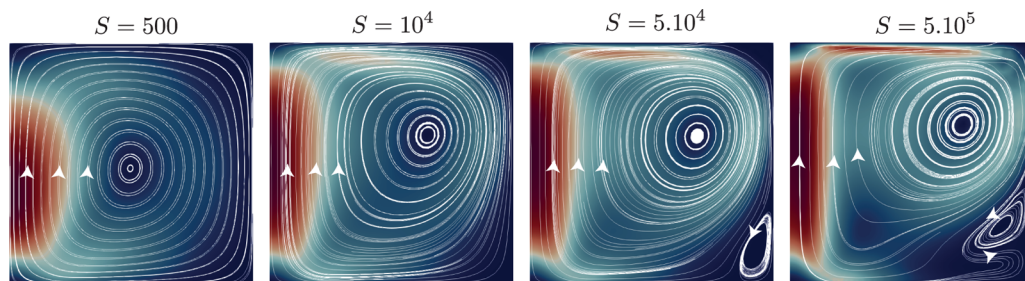

FIG. 8. Transition from viscous to inertial regime as S increases in axisymmetric computations. We show streamlines of the flow in meridional planes and the colors code the intensity. Millere boundary conditions, $P_m = 10^{-6}$ and $r_w = 0.2$.
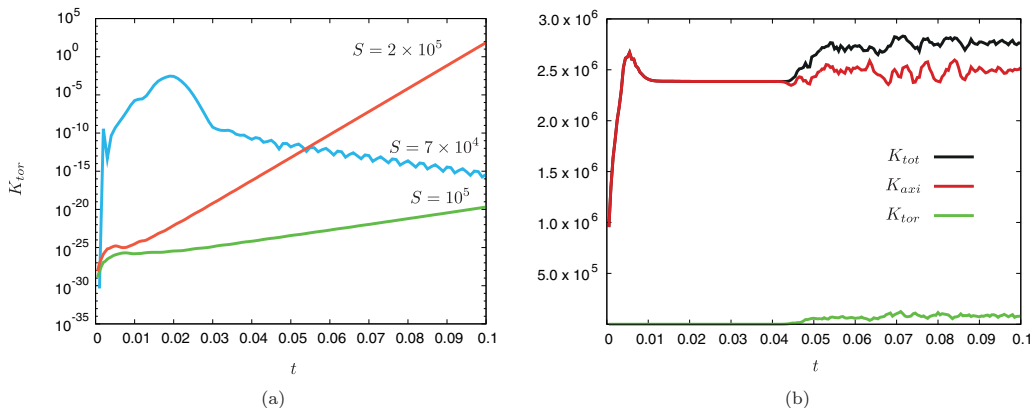
FIG. 9. Time evolution of the kinetic energy measures K_{tot}, K_{axi}, K_{tor} [see Eqs. (18a)–(18c)] in three-dimensional electrovortex flow simulations with wire, $\hat{\sigma} = 56$, $P_m = 1.57 \times 10^{-7}$. Initial state is axisymmetric. (a) Below $S < S_c = 7.2 \times 10^4$ the flow remains axisymmetric, above $S > S_c$ the flow becomes three-dimensional. This bifurcation is illustrated using the kinetic energy carried by the azimuthal component K_{tor} as proxy for three-dimensionality. Notice the decay or amplification for large times. (b) Simulation done with $S = 10^6$. The energy measures show that three-dimensionality comes along with nonstationarity. Notice that the total kinetic energy K_{tot} is higher in the three-dimensional regime than in the axisymmetric regime (i.e., for $t < 0.04$ when nonaxisymmetric perturbations are negligible).

simulations, the three-dimensional structure grow spontaneously out of the background numerical noise. A noticeable feature is that $u_{\theta,0} = 0$ always, i.e., there is never a significant azimuthal axisymmetric flow even in three-dimensional simulations.

To make diagnostics we calculate the total kinetic energy K_{tot}, the part of the kinetic energy carried by the azimuthal flow component K_{tor}, and the kinetic energy contained in the axisymmetric flow K_{axi}. Using the notations introduced in Eq. (3), we define

$$K_{\text{tot}} = \sum_{m=0}^{M-1}(1 + \delta_{m0})\frac{\pi}{2} \int_0^1 \int_0^1 \left(\left\| \boldsymbol{u}_m^c \right\|^2 + \left\| \boldsymbol{u}_m^s \right\|^2 \right) r \, dr \, dz, \tag{18a}$$

$$K_{\text{tor}} = \sum_{m=0}^{M-1}(1 + \delta_{m0})\frac{\pi}{2} \int_0^1 \int_0^1 \left(\left\| u_{\theta,m}^c \right\|^2 + \left\| u_{\theta,m}^s \right\|^2 \right) r \, dr \, dz, \tag{18b}$$

$$K_{\text{axi}} = \pi \int_0^1 \int_0^1 \left\| \boldsymbol{u}_0^c \right\|^2 r \, dr \, dz. \tag{18c}$$

The quantities K_{tor} and $K_{\text{tot}} - K_{\text{axi}}$ both provide simple measures of the three-dimensionality of the flow.

We have done a series of calculations in which we vary S in a configuration where a copper wire is connected to mercury ($\hat{\sigma} = 56$, $P_m = 1.57 \times 10^{-7}$). All the calculations are started from the axisymmetric state and three-dimensional numerical noises. Flow intensities that are reached here are never high enough to leave the low Rm regime. At low values of S, we observe that the electrovortex flow remains axisymmetric and stationary. Beyond a critical value $S = S_c$, we observe a bifurcation toward a time-dependent three-dimensional motion. This is illustrated in Fig. 9(a), where we show K_{tor} as a function of time. At $S = 7 \times 10^4$, K_{tor} decays exponentially, while for higher values of S, K_{tor} increases exponentially. We approximately locate the threshold of the three-dimensional instability at $S_c \approx 7.2 \times 10^4$.

Three-dimensionality is progressively more important as S increases, but it never becomes very strong in the range of values of S we have explored. The weakness of the three-dimensional effects is

TABLE II. Time-averaged values of the kinetic energy K_{tot}, axisymmetric kinetic energy K_{axi}, and ratio $(K_{\text{tot}} - K_{\text{axi}})/K_{\text{tot}}$.

$S/10^5$	$K_{\text{tot}}/10^5$	$K_{\text{axi}}/10^5$	$(K_{\text{tot}} - K_{\text{axi}})/K_{\text{tot}}$ [%]
3	8.186	7.783	4.90
4	11.10	10.42	6.19
5	14.45	13.07	9.56
10	28.48	24.90	12.6

visible in Fig. 9(b), where we show the time evolution of K_{tor}, K_{axi}, K_{tot} at $S = 10^6$. Table II further illustrates this observation; this table gathers some numerical measures for time-averaged values of K_{tot} and $(K_{\text{tot}} - K_{\text{axi}})/K_{\text{tot}}$ in the three-dimensional regime. At the highest value of S we have explored, only 12.6% of the kinetic energy is being carried by nonaxisymmetric modes.

In Fig. 10(a), we show a snapshot of the typical three-dimensional flow structure at $S = 3 \times 10^5$. The flow is predominantly axisymmetric, but we observe some weak azimuthal deviations in the streamlines. Figure 10(b) displays the maximal flow intensity and compares the 3D simulations with axisymmetric simulations. In the low S regime, the flow remains axisymmetric and nothing changes. At high S, the scaling law $u_{\text{max}} \sim \sqrt{S}$ observed in the axisymmetric simulations remains valid even with three-dimensional flow features present. Three-dimensionality slightly increases the flow's intensity as can be seen in Fig. 9(b) but this small increase is not visible in the logarithmic plot of Fig. 10(b)

D. Conclusion

The code SFEMaNS reproduces well all the quantitative and qualitative aspects of the electro-vortex flow that were previously known in the literature. The effect of a solid wire that brings the current to the liquid can be modeled correctly by using the uniform boundary condition provided the conductivity of the wire is small compared to that of the fluid. The Millere boundary condition is well suited if the conductivity of the wire is large compared to that of the fluid. The magnitude of the Lorentz force is very sensitive to the conductivity of the wire, but the component of the Lorentz force that effectively drives the electrovortex flow is not. The electrovortex flow predominantly remains axisymmetric up to very high values of S, and the usual low and high S scaling laws for the
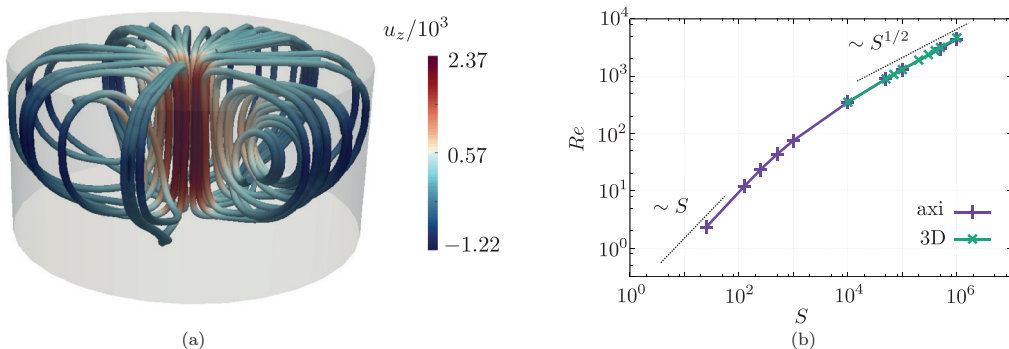

FIG. 10. (a) Snapshot showing streamlines of the three-dimensional electrovortex flow ($\hat{\sigma} = 56$, $P_m = 1.57 \times 10^{-7}$, $S = 3 \times 10^5$). (b) Maximal flow velocity as a function of S: comparison of 3D and axisymmetric simulations.
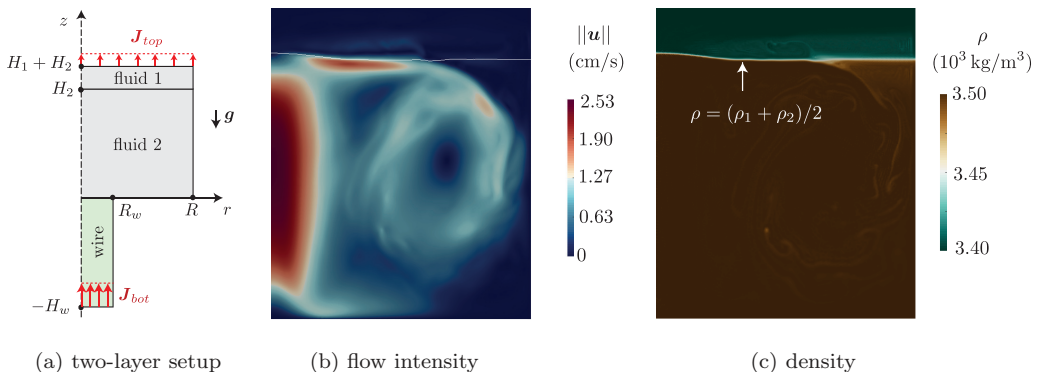
FIG. 11. Electrovortex flow in a two-layer setup in a small cell with radius $R = 5\,\mathrm{cm}$, wire radius $R_w = 1\,\mathrm{cm}$, heights $H_1 = 1\,\mathrm{cm}$, $H_2 = 5\,\mathrm{cm}$, $H_w = 5\,\mathrm{cm}$, current $I = 100\,\mathrm{A}$ and densities $\rho_1 = 3400\,\mathrm{kg\,m^{-3}}$, $\rho_2 = 3500\,\mathrm{kg\,m^{-3}}$. (a) Sketch of the setup. (b) Snapshot of the electrovortex flow. (c) Density field.

flow's intensity, or Reynolds number, remain valid in three-dimensional simulations and as long as the magnetic Reynolds number remains small compared to unity.

IV. ELECTROVORTEX FLOW IN MULTIPHASE SETUPS

After having characterized the electrovortex flow inside a single fluid layer, we now continue with the more complex case where the fluid is composed of multiple layers. First we investigate a two-layer configuration, then we investigate a three-layer configuration similar to that of a Mg-Sb liquid metal battery. The calculations are done using the multiphase version of SFEMaNS and in dimensional units. Since the electrovortex flow seems to be predominantly axisymmetric, all the multiphase results reported below are obtained assuming axisymmetry.

A. two-layer setup

We first study a purely academic two-layer setup, using material parameters and dimensions that are easily accessible to our numerical simulations. This allows us to identify simple physical behavior that will also be relevant to the three-layer Mg-Sb LMB simulated in the following section.

We sketch the numerical setup in Fig. 11(a). A homogeneous current density $\boldsymbol{J}_{\mathrm{bot}} = (I/\pi R_w^2)\boldsymbol{e}_z$ is fed to a copper wire of length $H_w = 5\,\mathrm{cm}$, radius $R_w = 1\,\mathrm{cm}$, and conductivity $\sigma_w = 58.1 \times 10^6\,\mathrm{S\,m^{-1}}$. The radius of the fluid domain is $R = 5\,\mathrm{cm}$ and there are two layers of superposed fluids. The height of the top layer is $H_1 = 1\,\mathrm{cm}$ and that of the bottom layer is $H_2 = 5\,\mathrm{cm}$. We consider two cases for the density of the top layer $\rho_1 \in \{3400, 3000\}\,\mathrm{kg\,m^{-3}}$, the density of the bottom layer is $\rho_2 = 3500\,\mathrm{kg\,m^{-3}}$. We suppose that the kinematic viscosities of the two layers are equal $\nu_1 = \nu_2 = 6.7 \times 10^{-7}\,\mathrm{m^2\,s^{-1}}$. The electrical conductivity of the top layer is $\sigma_1 = 10^4\,\mathrm{S\,m^{-1}}$ and that of the bottom layer is $\sigma_2 = 10^6\,\mathrm{S\,m^{-1}}$. The top layer has a significantly weaker conductivity than the bottom layer to mimic the situation that one encounters when in presence of a well-conducting heavy liquid metal and a badly conducting lighter electrolyte. The current leaves the top layer uniformly $\boldsymbol{J}_{\mathrm{top}} = (I/\pi R^2)\boldsymbol{e}_z$. Gravity acts downward, and we use $g = 9.81\,\mathrm{m\,s^{-2}}$.

Considering the geometry of this setup, it is mainly in the bottom layer that the electrical current spreads out. As a result, we expect the EVF phenomenon to occur in the bottom layer, and we expect the fluid in the top layer to be put in motion by viscous effects.

We start by considering the two-layer setup with $\rho_1 = 3400\,\mathrm{kg\,m^{-3}}$ and a current of $I = 100\,\mathrm{A}$ is driven through the cell. This gives $S = \mu_0 I^2/(4\pi^2 \rho_2 \nu_2^2) = 2 \times 10^5$ in the bottom layer. The numerical simulations show that after an initial transient, the flow settles in a quasi-stationary state very similar to what we have observed in Sec. III with one fluid layer for large values of S.
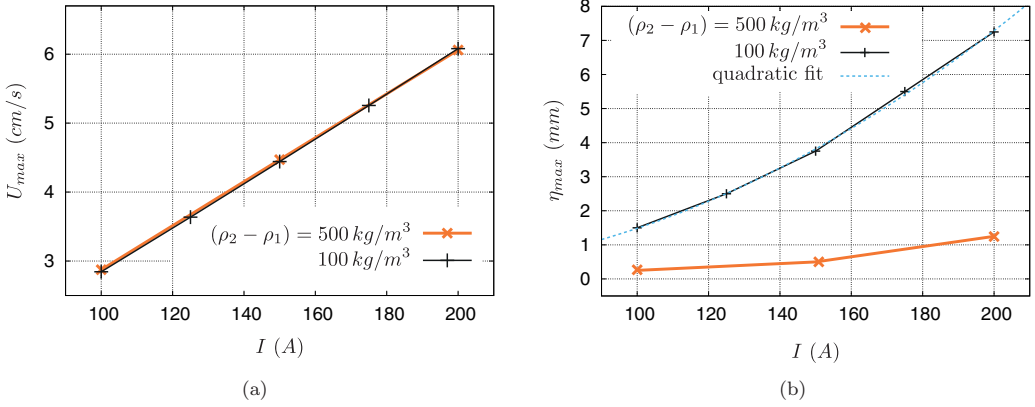
FIG. 12. Variation of the maximal flow speed $U_{\max}$ (a) and the maximal interface elevation $\eta_{\max}$ (b) with current I in the two-layer setup with $(R, R_w, H_1, H_2, H_w) = (5, 1, 1, 5, 5)$ cm and using two different density jumps $\rho_2 - \rho_1 \in \{100, 500\}$kg/m^3.

Figures 11(b) and 11(c) show snapshots of the intensity of the electrovortex flow and of the density field. The EVF slightly pushes the top fluid layer upward and deforms the interface. A weak flow is generated in the top layer as a reaction to the viscous constraints occurring at the interface. No horizontal gravity waves are observed.

We now perform a more systematic series of calculations and measure $U_{\max}$ and $\eta_{\max}$ the maximal flow speed and interface deformation reached over time and in the cell. We consider the two cases $\rho_1 \in \{3400, 3000\}$kg m^{-3} and we vary the current I in the range [100 A, 200 A]. The nondimensional quantity S spans the interval $[2 \times 10^5, 8 \times 10^5]$. Since S is very large we posit that the scaling law Re $\sim \sqrt{S}$ is likely to apply in the bottom layer; hence in dimensional form we should have

$$U_{\max} \sim \frac{\sqrt{\mu_0}I}{\sqrt{\rho_2}R}. \tag{19}$$

We show in Fig. 12(a) the quantity $U_{\max}$ (estimated numerically with SFEMaNS) as a function of I for the two densities $\rho_1 \in \{3400, 3000\}$ kg m^{-3}. The proportionality of $U_{\max} \sim I$ is clearly visible on the graphs. Since the two curves almost coincide, this test shows that the density of the top layer, ρ_1, has very little impact on $U_{\max}$. We show in Fig. 12(b) the maximal elevation of the interface, $\eta_{\max}$, caused by the electrovortex flow, as a function of I. The curves are well approximated by parabolas. This can be explained by balancing the available kinetic energy density in the bottom layer $\rho_2 U_{\max}^2/2$ with the potential energy density $(\rho_2 - \rho_1)g\eta_{\max}$ required to deform the interface:

$$\eta_{\max} \approx \frac{\rho_2 U_{\max}^2}{2(\rho_2 - \rho_1)g} \xrightarrow{Eq.(19)} \eta_{\max} \approx \frac{\mu_0 I^2}{2(\rho_2 - \rho_1)gR^2}. \tag{20}$$

This suggests that the maximal surface elevation varies like I^2 and only depends on the density difference. A similar scaling for the interface deformation was also observed by the authors of Ref. [41], who considered EVF in a free surface setup. In nondimensional form, this suggests a Richardson number

$$\text{Ri} = \frac{2(\rho_2 - \rho_1)g\eta_{\max}}{\rho_2 U_{\max}^2} \approx 1. \tag{21}$$

For all the simulations reported in Fig. 12, we have measured Ri $= 1.05 \pm 0.05 \approx 1$ (data not shown). This observation implies that the above criterium [or Eq. (20)] makes sense as a simple formula to estimate $\eta_{\max}$.
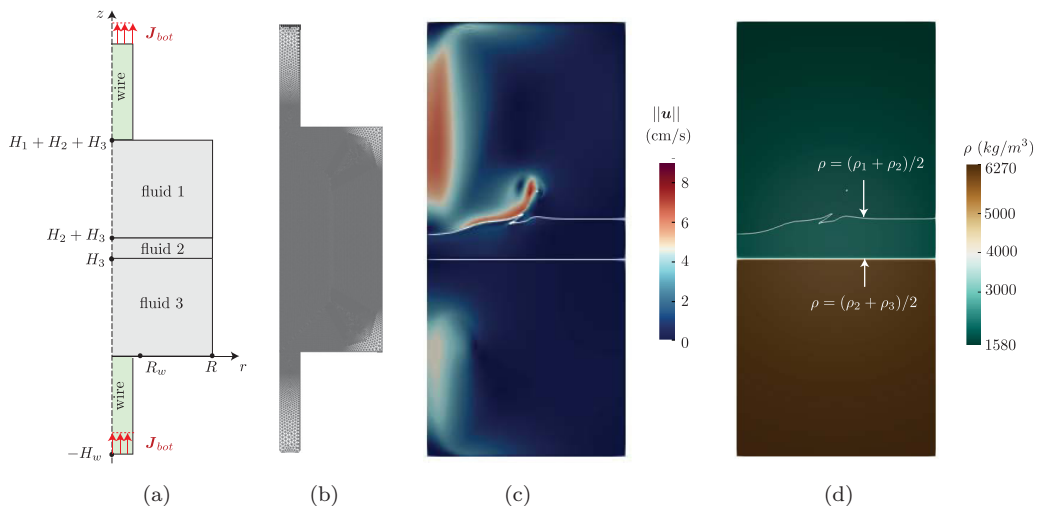
FIG. 13. Electrovortex flow in a three-layer setup similar to a Mg-Sb liquid metal battery. Small cell with radius $R = 5$ cm, wire radius $R_w = 1$ cm, heights $(H_1, H_2, H_3, H_w) = (5, 1, 5, 5)$ cm, and densities $(\rho_1, \rho_2, \rho_3) = (1577, 1715, 6270)$ kg m^{-3}. (a) Sketch of the setup. (b) Meridional grid with mesh size $\in$ [0.25, 1]mm. (c), (d) Snapshot of the electrovortex flow and density field at $t = 2$ s with current $I = 200$ A.

B. Three-layer setup: Liquid metal battery

We now consider a three-layer setup typical for a Mg-Sb liquid metal battery [1]. A sketch of the simulated system is shown in Fig. 13. We fix the radius to be $R = 5$ cm and the heights of three layers to be $(H_1, H_2, H_3) = (5, 1, 5)$ cm. Both solid electrodes have radii $R_w = 1$ cm and have height $H_w = 5$ cm. A homogeneous current density enters the fluid bath through the bottom electrode and exits through the top electrode. The top and bottom fluid layers are composed of liquid metals, one light (fluid 1: Mg) and one heavy (fluid 3: Sb, which alloys with Mg). The layer in between is an electrolyte [fluid 2: molten salt (KCl-MgCl$_2$-NaCl)]. The densities of the three fluids are chosen to make the system stable under gravity. The material parameters for the three different fluids used in our simulations are given in Table III and are realistic.

Considering the geometry of the electrodes, we expect the EVF to occur in the top and the bottom layers. As in the two-layer setup, the fluid composing the electrolyte layer is only entrained by viscosity; therefore, we expect the motion of the fluid to be weak in this layer. We seek to drive an intense EVF and therefore vary the current intensity I in the range [100, 300] A. In our small setup, the initial current density $\boldsymbol{J} \approx J\boldsymbol{e}_z$ reaches magnitudes $J = I/\pi R^2 \in [12.7, 38.1]$ kAm^{-2} well above what can be handled by existing Mg-Sb LMBs. Below, we explain how the principle of similitude can be used to extrapolate our results to more realistic setups with realistic J.

In Fig. 13(b), we show the fine numerical mesh used in our calculations. Figures 13(c) and 13(d) show a snapshot of the flow and density fields for the current $I = 200$ A, taken at the time $t = 2$ s

TABLE III. Density ρ_i, dynamic viscosity $\rho_i\nu_i$, conductivity σ_i, and magnetic Prandtl number $P_{m,i}$ of the three fluids $i = 1, 2, 3$ composing a Mg-Sb liquid metal battery [11].

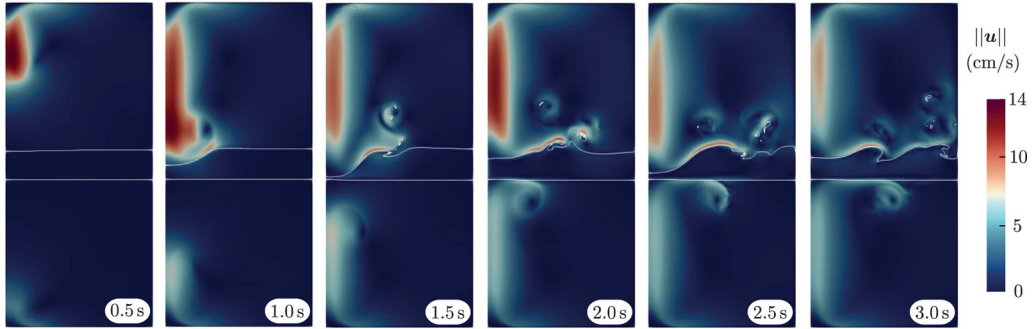| Fluid	ρ_i [kg m^{-3}]	$\rho_i\nu_i$ [Pag s]	σ_i [S m^{-1}]	$P_{m,i}$
1 (Mg)	1.577×10^3	1.23×10^{-3}	3.57×10^6	3.499×10^{-6}
2 (KCl-MgCl$_2$-NaCl)	1.715×10^3	1.40×10^{-3}	2.13×10^2	2.626×10^{-8}
3 (Sb)	6.270×10^3	1.30×10^{-3}	2.56×10^6	6.670×10^{-7}

FIG. 14. When the electrovortex flow in a Mg-Sb battery becomes too intense, it can make the electrolyte layer to pinch. In the cell considered here, this occurs at $I = 300$ A. Starting from rest at $t = 0$ s, we show six successive snapshots of the flow intensity and the interfaces at indicated times.

with the fluid being at rest at $t = 0$ s. The flow in the top layer is (somewhat surprisingly) more intense than in the bottom layer. But, following Eq. (19), we expect $U_{\max} \sim \sqrt{\mu_0} I / \sqrt{\rho_i} R$, $i = 1, 3$, in the top and the bottom layers; hence, recalling that $\frac{\rho_1}{\rho_3} \sim \frac{1}{4}$, the above formula suggests that the fluid motion in the top layer should be approximately two times faster than the fluid motion in the bottom layer. We also observe the interface between the top layer and the electrolyte, henceforth denoted 1|2, undergoes deformations while the interface between the electrolyte and the bottom layer, henceforth denoted 2|3, remains almost flat. This is mainly due to the fact that the density jump across the 1|2 interface is weak ($\rho_2 - \rho_1 = 138 \, \mathrm{kg m}^{-3}$ and $\frac{\rho_2 - \rho_1}{\rho_1} \sim 0.08$), whereas the density jump across the 2|3 is large ($\rho_3 - \rho_2 = 4555 \, \mathrm{kg m}^{-3}$ and $\frac{\rho_3 - \rho_2}{\rho_3} = 0.75$). According to Eq. (20) the maximum deformation $\eta_{\max}$ of the 1|2 interface can approximately be $\frac{4555}{138} \sim 33$ times larger than that of the 2|3 interface.

At $I = 200$ A the interface deformation is very large, but with an even more intense current, $I = 300$ A, we find that the electrovortex flow is so vigorous that it can cause the electrolyte layer to pinch, thereby creating a short circuit between the two metallic phases. This situation must be avoided in real LMBs because the cell potential is lost and violent chemical reactions may make the cell unsafe. Figure 14 shows six snapshots of this simulated electrolyte pinch. The time between each picture is 0.5 s and the simulation started from rest. The downward jet in the upper layer hits the 2|3 interface violently, causing electrolyte to splash into the top layer. We recall here that that three-dimensional and the capillarity effects are not simulated. These effects would very likely modify the flow, but we are confident that the initial stage of the splashing is well captured by our axisymmetric numerical simulation. Further quantitive information on the evolution of maximal speed $U(t)$ and upper interface deformation $\eta(t)$ in the cell as a function of time is given in Fig. 15(a) (green lines, real σ_2, black lines, fake σ_2). These plots show that through time, the highest flow speed $U_{\max} = \max_t [U(t)]$ and largest interface deformation $\eta_{\max} = \max_t [\eta(t)]$ are reached during the initial transient. At later times, the flow never reaches the same intensity as in the beginning and the same for the interface deformation. Notice also the oscillations in the interface deformation that reflect the presence of gravity waves driven by the initial push.

In the simulation for $I = 300$ A that has just been discussed, fine fluid structures combine with large jumps in electrical conductivity, $\sigma_1/\sigma_2 = O(10^4)$, $\sigma_3/\sigma_2 = O(10^4)$. As a result, this is a very stiff problem to solve numerically that requires very fine grids and tiny time steps to keep the simulation stable. In previous work [19] on the metal pad roll instability, we have shown that the relaxation of the conductivity of the electrolyte to $\sigma_2 = \sigma_3/100$ did not affect the main fluid mechanical features. This decreased jump in conductivity is easier to simulate and is a time-saving trick to do more extensive parameter studies in LMBs. In Fig. 15, we study the impact of using such a fake, artificially high value of σ_2 in the high current simulation with $I = 300$ A. In Fig. 15(a), we
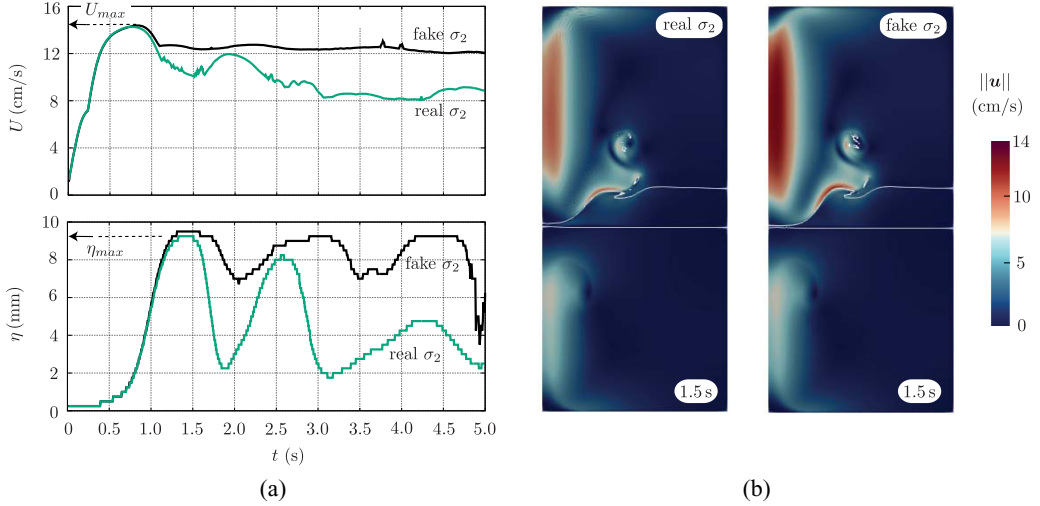
FIG. 15. Simulations with realistic values of electrolyte conductivity $\sigma_2 = 2.13 \, 10^2 \, \mathrm{S \, m^{-1}}$ versus simulations with relaxed (fake) electrolyte conductivity $\sigma_2 = 2.56 \, 10^4 \, \mathrm{S \, m^{-1}} = \sigma_3/100$ and with intense currents $I = 300 \, \mathrm{A}$. (a) The maximal speed and interface deformation are significantly affected at longer times, but the initial maxima are always the highest ones and these values depend little on σ_2 (arrows). (b) At short times $t = 1.5 \, \mathrm{s}$, the flow is similar and slightly more intense with higher σ_2.

can see how the initial phase of the dynamics is nearly unaffected. The quantities $U_{\max}$ and $\eta_{\max}$ can be measured correctly up to a few percent in error, using the fake value of $\sigma_2 = \sigma_3/100$. At later times, we do see that the use of a fake value for σ_2 can cause significant differences at high currents. This is less the case for low currents. Figure 15(b) compares snapshots of the flow at short time $t = 1.5 \, \mathrm{s}$, to confirm that the initial flow evolution is rather similar with the fake value of σ_2. At later times, we found that it is mainly the splashing dynamics creating the fine fluid structures that is sensitive to σ_2, but this process is anyway not correctly solved without capillarity.

We now present results from a more extensive simulation campaign that focused on $U_{\max}$ and $\eta_{\max}$ for varying currents in the range $I \in [100, 300] \, \mathrm{A}$. Considering the previous test, we can use $\sigma_2 = \sigma_3/100$ to measure $U_{\max}$ and $\eta_{\max}$ and this reduces the computational effort. Figure 16(a) shows that the data-points follow the same linear and quadratic laws as in the two-layer setup. The last data point for $\eta_{\max}$ at $I = 300 \, \mathrm{A}$ clearly deviates from the quadratic fit because the electrolyte pinches.

We now remap the data in nondimensional form using the definitions

$$\Pi = \frac{\sqrt{\rho_1} R U_{\max}}{\sqrt{\mu_0} I}, \quad \mathrm{Ri} = \frac{2(\rho_2 - \rho_1) g \eta_{\max}}{\rho_1 U_{\max}^2}, \tag{22}$$

and show in Fig. 16(b) Π and Ri as functions of $S := \frac{\mu_0 I^2}{4\pi^2 \rho_1 \nu_1^2}$. The two nondimensional parameters Π and Ri vary weakly with respect to S and they are both of order 1. The number Π seems to tend toward the asymptotic value 0.86 ± 0.01 when S becomes very large. As in the two-layer setup, we observe that $\mathrm{Ri} \gtrsim 1$ in all the nonpinching configurations.

Using the principle of similitude, we use the data obtained above to make some predictions for upscaled Mg-Sb cells composed of the same materials and with the same geometrical aspect ratios as above. Dimensional variables without bars, $R, U_{\max}, \eta_{\max}, \ldots$, correspond to the previously mentioned *reference* setup. Variables with bars, $\overline{R}, \overline{U}_{\max}, \overline{\eta}_{\max}, \ldots$, correspond to *similar* setups. As in Ref. [11], we want to take into account that the electrical current density is bounded from above by physical limits on the mass transfer between the electrolyte and the alloy in the bottom
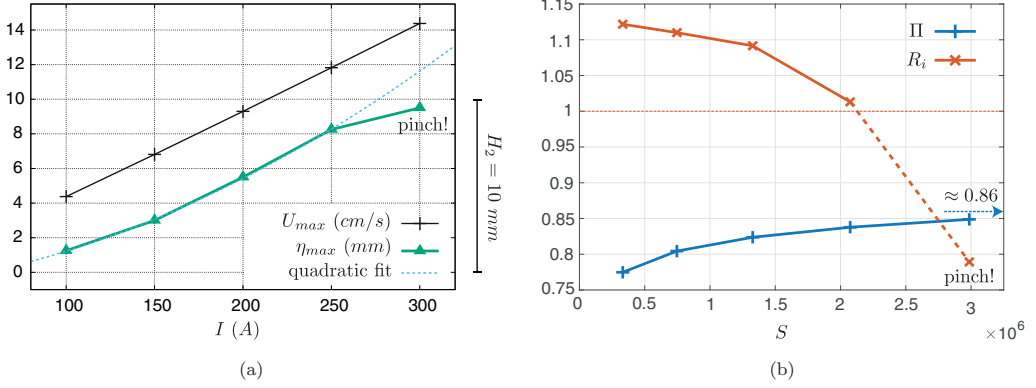
FIG. 16. (a) Maximal flow intensity $U_{\max}$ and upper interface deformation $\eta_{\max}$ as a function of I in a Mg-Sb battery with dimensions $(R, R_w, H_1, H_2, H_3, H_w) = (5, 1, 5, 1, 5, 5)$ cm. We observe $U_{\max} \sim I$ and $\eta_{\max} \sim I^2$. At the highest current $I = 300$ A we observe a pinch: $\eta_{\max} \approx H_2$. (b) nondimensional parameters Π and Ri as a function of S using the data in (a) [see Eq. (22)].

layer [2,4]. In the reference setup, the current density $\boldsymbol{J} \approx J\boldsymbol{e}_z$ is approximately homogeneous with $J = I/\pi R^2 \in [12.7, 38.1]$ kAm^{-2} for $I \in [100, 300]$ A. These values for J are above what can be reached in existing Mg-Sb LMBs. Therefore, we consider three scenarios $\overline{J} \in \{1, 3, 10\}$ kAm^{-2} in the *similar* setups. The first two values are realistic for Mg-Sb batteries [1,4], however, 10 kAm^{-2} is closer to what can be reached in Li-Sb(Pb) cells [3]. Requiring similitude on S (or electrical current I) implies $I = \overline{I}$, which gives I as a function of $\overline{R}$:

$$I(\overline{R}) = \pi \overline{J} \, \overline{R}^2. \tag{23}$$

Requiring similitude on the number Π (or Reynolds number Re) implies that $\overline{U}_{\max} = U_{\max} \frac{R}{\overline{R}}$. Since $U_{\max}$ is a function of I, we infer the dependency of $\overline{U}_{\max}$ with respect of $\overline{R}$ as follows:

$$\overline{U}_{\max}(\overline{R}) = U_{\max}[I(\overline{R})] \frac{R}{\overline{R}}. \tag{24}$$

Requiring similitude on Ri implies that $\overline{\eta}_{\max} = \eta_{\max} \frac{\overline{U}_{\max}^2}{U_{\max}^2} = \eta_{\max} \frac{R^2}{\overline{R}^2}$. Since $\eta_{\max}$ is a function of I, we can express $\overline{\eta}_{\max}$ as a function of $\overline{R}$ as follows:

$$\overline{\eta}_{\max}(\overline{R}) = \eta_{\max}[I(\overline{R})] \frac{R^2}{\overline{R}^2}. \tag{25}$$

The two functions $\overline{U}_{\max}(\overline{R})$ and $\overline{\eta}_{\max}(\overline{R})$ are displayed in Fig. 17 for the three scenarios $\overline{J} \in \{1, 3, 10\}$ kAm^{-2}. Since we observed that $U_{\max}$ is approximately linear with respect to I, say $U_{\max} \approx \alpha I$, we infer that $\overline{U}_{\max}(\overline{R}) \approx \alpha \pi \overline{J} R \overline{R}$, i.e., $\overline{U}_{\max}$ is also approximately linear with respect to $\overline{R}$. Similarly, using that $\eta_{\max} \approx \beta I^2$, we infer that $\overline{\eta}_{\max}(\overline{R}) \approx \beta \pi^2 \overline{J}^2 R^2 \overline{R}^2$, i.e., $\overline{\eta}_{\max}$ is also approximately quadratic in $\overline{R}$. Notice that the slope for $\overline{U}_{\max}$ behaves like $\overline{J}$ and the upward curvature of $\overline{\eta}_{\max}$ behaves like $\overline{J}^2$.

The plots of Fig. 17 were made supposing perfect similitude between the *reference* and the *similar* setups, but the exact similitude constraint can be relaxed. The geometrical similitudes $R_w/R = \overline{R}_w/\overline{R} = 0.2$ and $H_1/R = \overline{H}_1/\overline{R} = 1$ directly affects the intensity of the flow in the top layer and cannot be relaxed. However, we conjecture that we should get almost the same curves as in Fig. 17 if the aspect ratios of the electrolyte layer are not similar, i.e., $\frac{\overline{H}_2}{\overline{R}} \neq \frac{H_2}{R}$. This conjecture is based on the fact that a change in $\overline{H}_2$ is likely not to affect the current density distribution
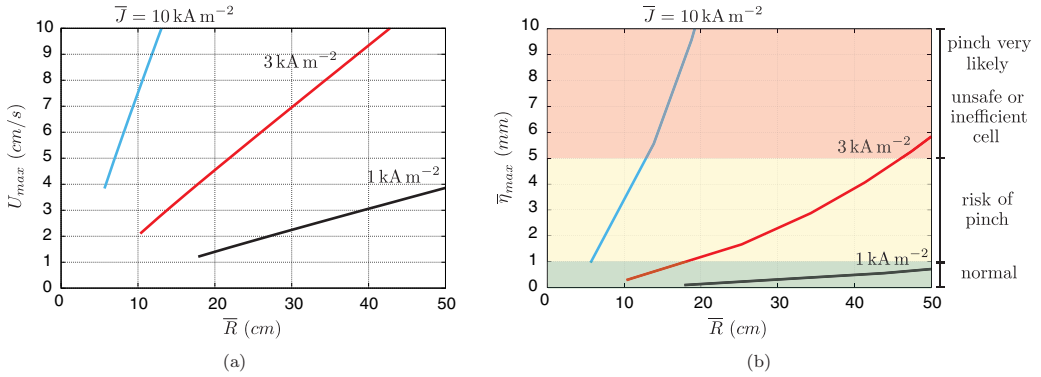
FIG. 17. Using the principle of similitude we calculate the maximal flow-speed $\overline{U}_{\max}$ (a) and the maximal interface elevation $\overline{\eta}_{\max}$ (panel b) in similar Mg-Sb liquid metal batteries as a function of their radius $\overline{R}$ for the current density $\overline{J} \in \{1, 3, 10\} \, \mathrm{kAm^{-2}}$. Assuming that the dependence with respect to the height of the electrolyte layer, $\overline{H}_2$, is small and taking $\overline{H}_2 \in [1, 5]$ mm, we divide the diagram for $\overline{\eta}_{\max}$ into three regions. No risk of pinch by EVF when $\overline{\eta}_{\max} < 1$ mm (green zone). Risk of pinch by EVF when $\overline{\eta}_{\max} \in [1, 5]$ mm (yellow zone). EVF-induced pinch very likely when $\overline{\eta}_{\max} > 5$ mm (red zone).

in the upper layer, which we recall is the source of the EVF flow. Let us reinterpret the $\overline{\eta}_{\max}$ diagram in Fig. 17(b) in this context, and let us suppose that the electrolyte has a realistic height $\overline{H}_2 \in [1, 5]$ mm. Then, the EVF is probably not strong enough to pinch the electrolyte in the cell when $\overline{\eta}_{\max}$ is below 1 mm (in the green band). There is a risk of short circuits induced by the EVF when $\overline{\eta}_{\max} \in [1, 5]$ mm (in the yellow band). Finally, it is very likely that the EVF is strong enough to make the electrolyte layer to pinch when $\overline{\eta}_{\max} > 5$ mm (in the red band). Overall, it seems from this diagram that the EVF phenomenon needs to be accounted for in the design of LMBs. Intense flows may occur in small size batteries and the risk of flow-induced short circuits is real.

V. CONCLUSION

The electrovortex flow is a well known magnetohydrodynamical phenomenon that occurs near every thin electrode that is connected to a liquid metal [22]. With the numerical code SFEMaNS, we have done axisymmetric and nonaxisymmetric simulations of the EVF in cylindrical fluid domains. We have explored configurations composed of one liquid metal and configurations composed of two and three layers with multiphase setups similar to those in liquid metal batteries.

In the single fluid layer study, we have reproduced several well known features of the electro-vortex flow, namely the flow structure and the scaling laws for the flow's intensity. The impact of the solid electrode carrying the electrical current to the cell can be modeled by using simplified boundary conditions when the wire's conductivity is either significantly larger (Millere boundary condition) or significantly smaller (uniform boundary condition) than that of the liquid metal. Three-dimensional simulations of the EVF for high values of S show that the flow is time-dependent but is also strongly dominated by its axisymmetric component.

In the multiphase study we have considered the EVF phenomenon in cells with either two or three layers of conducting fluids that are stably stratified by gravity. The EVF is generated in the vicinity of the contact between the solid electrodes and the liquid metals. The flow has roughly the same structure and intensity as in single fluid layers. The interfaces between the different phases are deformed by the flow. A simple energy density balance yields a reasonable estimate of the maximal deformation of the interface. When using the material properties of Mg-Sb liquid metal batteries, we have shown that the electrovortex phenomenon cannot be ignored. Already in moderate size batteries it seems possible to have flows that are sufficiently intense to pinch the thin electrolyte layer. Compared to thermal convection [4–6,8], the Tayler instability [9–11], and the metal pad roll

instability [12–19], this study suggests that the electrovortex can produce a fluid flow capable of disrupting the integrity of the upper interface.

In the future, we plan to explore whether the electrovortex flow in liquid metal batteries could be a useful ally to overcome the limitations on the current density. As in all galvanic batteries, transport of charge (current) comes along with a transport of mass between the top and the bottom metal across the electrolyte. But when intense currents are extracted from (or delivered to) the cell, the alloy may become quite inhomogeneous near the alloy-electrolyte interface. This causes the battery to lose its potential or may even trigger the appearance of undesirable solid intermetallic phases. Just as natural convection [4], the electrovortex flow has the capacity to mix the bottom alloy [7,20] and we need to asses if this is indeed possible or not.

ACKNOWLEDGMENTS

[1] D. J. Bradwell, H. Kim, A. H. C. Sirk, and D. R. Sadoway, Magnesium-antimony liquid metal battery for stationary energy storage, J. Am. Chem. Soc. **134**, 1895 (2012).

[2] H. Kim, D. A. Boysen, T. Ouchi, and D. R. Sadoway, Calcium-bismuth electrodes for large-scale energy storage (liquid metal batteries), J. Power Sources **241**, 239 (2013).

[3] K. Wang, K. Jiang, B. Chung, T. Ouchi, P. J. Burke, D. A. Boysen, D. J. Bradwell, H. Kim, U. Muecke, and D. R. Sadoway, Lithium-antimony-lead liquid metal battery for grid-level energy storage, Nature **514**, 348 (2014).

[4] D. H. Kelley and D. R. Sadoway, Mixing in a liquid metal electrode, Phys. Fluids **26**, 057102 (2014).

[5] Y. Shen and O. Zikanov, Thermal convection in a liquid metal battery, Theor. Comput. Fluid Dyn. **30**, 275 (2016).

[6] T. Köllner, T. Boeck, and J. Schumacher, Thermal Rayleigh-Marangoni convection in a three-layer liquid-metal-battery model, Phys. Rev. E **95**, 053114 (2017).

[7] R. F. Ashour, D. H. Kelley, A. Salas, M. Starace, N. Weber, and T. Weier, Competing forces in liquid metal electrodes and batteries, J. Power Sources **378**, 301 (2018).

[8] P. Personnettaz, P. Beckstein, S. Landgraf, T. Köllner, M. Nimtz, N. Weber, and T. Weier, Thermally driven convection in Li ∥ Bi liquid metal batteries, J. Power Sources **401**, 362 (2018).

[9] N. Weber, V. Galindo, F. Stefani, and T. Weier, Current-driven flow instabilities in large-scale liquid metal batteries, and how to tame them, J. Power Sources **265**, 166 (2014).

[10] N. Weber, V. Galindo, J. Priede, F. Stefani, and T. Weier, The influence of current collectors on Tayler instability and electrovortex flows in liquid metal batteries, Phys. Fluids **27**, 014103 (2015).

[11] W. Herreman, C. Nore, L. Cappanera, and J.-L. Guermond, Tayler instability in liquid metal columns and liquid metal batteries, J. Fluid Mech. **771**, 79 (2015).

[12] O. Zikanov, Metal pad instabilities in liquid metal batteries, Phys. Rev. E **92**, 063021 (2015).

[13] N. Weber, P. Beckstein, W. Herreman, G. M. Horstmann, C. Nore, F. Stefani, and T. Weier, Sloshing instability and electrolyte layer rupture in liquid metal batteries, Phys. Fluids **29**, 054101 (2017).

[14] N. Weber, P. Beckstein, V. Galindo, W. Herreman, C. Nore, F. Stefani, and T. Weier, Metal pad roll instability in liquid metal batteries, Magnetohydrodynamics **53**, 129 (2017).

[15] V. Bojarevics and A. Tucs, MHD of large scale liquid metal batteries, *Light Metals 2017* (Springer, Cham, 2017), pp. 687–692.

[16] G. M. Horstmann, N. Weber, and T. Weier, Coupling and stability of interfacial waves in liquid metal batteries, J. Fluid Mech. **845**, 1 (2018).

[17] S. Molokov, The nature of interfacial instabilities in liquid metal batteries in a vertical magnetic field, Europhys. Lett. **121**, 44001 (2018).

[18] O. Zikanov, Shallow water modeling of rolling pad instability in liquid metal batteries, Theor. Comput. Fluid Dyn. **32**, 325 (2018).

[19] W. Herreman, C. Nore, J.-L. Guermond, L. Cappanera, N. Weber, and G. M. Horstmann, Perturbation theory for metal pad roll instability in cylindrical reduction cells, J. Fluid Mech. 878, 598 (2019).

[20] N. Weber, M. Nimtz, P. Personnettaz, A. Salas, and T. Weier, Electromagnetically driven convection suitable for mass transfer enhancement in liquid metal batteries, Appl. Therm. Eng. **143**, 293 (2018).

[21] D. H. Kelley and T. Weier, Fluid mechanics of liquid metal batteries, Appl. Mech. Rev. **70**, 020801 (2018).

[22] V. Bojarevics, J. A. Freibergs, E. I. Shilova, and E. V. Shcherbinin, *Electrically Induced Vortical Flows*, (Kluwer Academic Publishers, Dordrecht, 1989).

[23] J. A. Shercliff, Fluid motions due to an electric current source, J. Fluid Mech. **40**, 241 (1969).

[24] L. Cappanera, J.-L. Guermond, W. Herreman, and C. Nore, Momentum-based approximation of incompressible multiphase fluid flows, Int. J. Numer. Methods Fluids **86**, 541 (2018).

[25] R. P. Millere, V. I. Sharamkin, and É. V. Shcherbinin, Effect of a longitudinal magnetic field on electrically driven rotational flow in a cylindrical vessel, Magnetohydrodynamics **16**, 66 (1980).

[26] J.-L. Guermond, R. Laguerre, J. Léorat, and C. Nore, An interior penalty Galerkin method for the MHD equations in heterogeneous domains, J. Comput. Phys. **221**, 349 (2007).

[27] J.-L. Guermond, R. Laguerre, J. Léorat, and C. Nore, Nonlinear magnetohydrodynamics in axisymmetric heterogeneous domains using a Fourier/finite element technique and an interior penalty method, J. Comput. Phys. **228**, 2739 (2009).

[28] C. Nore, D. Castanon Quiroz, L. Cappanera, and J.-L. Guermond, Direct numerical simulation of the axial dipolar dynamo in the Von Kármán sodium experiment, Europhys. Lett. **114**, 65002 (2016).

[29] A. Giesecke, C. Nore, F. Stefani, G. Gerbeth, J. Léorat, W. Herreman, F. Luddens, and J.-L. Guermond, Influence of high-permeability discs in an axisymmetric model of the Cadarache dynamo experiment, New J. Phys. **14**, 053005 (2012).

[30] N. Weber, P. Beckstein, V. Galindo, M. Starace, and T. Weier, Electrovortex flow simulation using coupled meshes, Comput. Fluids **168**, 101 (2018).

[31] A. Bonito and J.-L. Guermond, Approximation of the eigenvalue problem for the time harmonic Maxwell system by continuous Lagrange finite elements, Math. Comp. **80**, 1887 (2011).

[32] A. Giesecke, C. Nore, F. Stefani, G. Gerbeth, J. Léorat, F. Luddens, and J.-L. Guermond, Electromagnetic induction in nonuniform domains, Geophys. Astrophys. Fluid Dyn. **104**, 505 (2010).

[33] A. Bonito, J.-L. Guermond, and F. Luddens, Regularity of the Maxwell equations in heterogeneous media and Lipschitz domains, J. Math. Anal. Appl. **408**, 498 (2013).

[34] I. E. Butsenieks, D. E. Peterson, V. I. Sharamkin, and E. V. Sherbinin, Magnetohydrodynamic fluid flows in a closed space with a nonuniform electric current, Magnetohydrodynamics **12**, 70 (1976).

[35] V. K. Vlasyuk, Effects of fusible-electrode radius on the electrovortex flow in a cylindrical vessel, Magnetohydrodynamics **23**, 434 (1987).

[36] A. Y. Chudnovskii, Evaluating the intensity of a single class of electrovortex flows MHD, Magnetohydrodynamics **25**, 406 (1989).

[37] P. A. Nikrityuk, K. Eckert, R. Grundmann, and Y. S. Yang, An impact of a low voltage steady electrical current on the solidification of a binary metal alloy: A numerical study, Steel Res. Int. **78**, 402 (2007).

[38] C. Kasprzyk, Numerische Untersuchung zur strömungsmechanik in flüssigmetallbatterien, Master thesis, Technische Universität Dresden, 2015.

[39] V. G. Zhilin, Y. P. Ivochkin, A. A. Oksman, G. R. Lurin'sh, A. I. Chaikovskii, A. Y. Chudnovskii, and E. V. Shcherbinin, An experimental investigation of the velocity field in an axisymmetric electrovortical flow in a cylindrical container, Magnetohydrodynamics **22**, 323 (1986).

[40] L. A. Volokhonskii, F. I. Gamzaev, S. B. Dement'ev, K. A. Zvyagin, and E. V. Shcherbinin, Dynamic boundary layer of electrovortex flow in a cylindrical volume with axisymmetric current supply, Magnetohydrodynamics **27**, 467 (1991).

[41] A. Kharicha, I. Teplyakov, Yu. Ivochkin, M. Wu, A. Ludwig, and A. Guseva, Experimental and numerical analysis of free surface deformation in an electrically driven flow, Exp. Therm. Fluid Sci. **62**, 192 (2015).